Characterizing the role of non-linear interactions in the transition to submesoscale dynamics at a dense filament

Mara Freilich[1], Luc Lenain[1], Sarah T. Gille[1]

[1]Scripps Institution of Oceanography, University of California San Diego

Key Points:

- Remote sensing observations reveal a kinetic energy spectrum with a continuous slope from 100 km to 1 km in an eastern boundary region.
- Between 1 and 10 km, ageostrophic non-linear interactions become dynamically important
- Cross-scale kinetic energy transfers computed from 2D velocity observations are associated with shear strain in the observed front.

Corresponding author: Mara Freilich, `mfreilich@ucsd.edu`

Abstract

Ocean dynamics at the submesoscale play a key role in mediating upper-ocean energy dissipation and dispersion of tracers. Observations of ocean currents from synoptic mesoscale surveys at submesoscale resolution (250 m–100 km) from a novel airborne instrument (MASS DoppVis) reveal that the kinetic energy spectrum in the California Current System is nearly continuous from 100 km to sub-kilometer scales, with a k^{-2} spectral slope. Although there is not a transition in the kinetic energy spectral slope, there is a transition in the dynamics to non-linear ageostrophic interactions at scales of $\mathcal{O}(1$ km). Kinetic energy transfer across spatial scales is enabled by interactions between the rotational and divergent components of the flow field at the submesoscale. Kinetic energy flux is patchy and localized at submesoscale fronts. Kinetic energy is transferred both downscale and upscale from 1 km in the observations of a cold filament.

Plain Language Summary

Ocean dynamics at scales of 100 m–10 km, called the submesoscale, are important because they are associated with large velocity gradients and non-linear interactions. Large gradients lead to vertical velocity, which facilitates ocean-atmosphere interactions and ocean biological processes. Velocity gradients and non-linear processes combine to transfer kinetic energy from the large-scale flow to small-scale perturbations. This can lead to instabilities that dissipate energy in the ocean surface layer (rather than the seafloor). Here we analyze novel observations that provide insight into ocean dynamics through the distributions of velocity gradients and energy transfer at 1 km scale. Dynamics at these scales have previously been modeled, but have not been observed directly. We observe a transition where non-linear dynamics become more important at scales of order 10 km. We also introduce new interpretations of spectral analysis (analysis of energy and correlations across scales). Moreover, we analyze covariance of velocity gradient quantities and flow energetics to demonstrate that energy flux is episodic and localized at fronts. Together, these observations demonstrate that fronts play an important role in boundary-layer kinetic energy processes and highlight the evolution of upwelling filaments.

1 Introduction

Ocean processes in the surface boundary layer play a critical role in mediating the influence of atmospheric and climate processes on the ocean. Heating, wind-driven momentum input, and gas exchange occur at the sea surface and are transmitted through the boundary layer and into the ocean interior. The boundary layer also resides in the photic zone, where there is enough light for photosynthesis.

Submesoscale dynamics, the dynamics that operate at the spatial scales between the nearly geostrophically balanced mesoscale eddies ($\sim$100 km scales in mid-latitudes) and three-dimensional turbulence ($<$ 100 m scales), are particularly important for these boundary layer processes (McWilliams, 2016). Submesoscales influence ocean biogeochemistry by modulating vertical transport (Mahadevan, 2016; Freilich et al., 2022) and influence air-sea interactions by modulating buoyancy and momentum transfer (Strobach et al., 2022). Submesoscale dynamics are hypothesized to facilitate a forward cascade of kinetic energy resulting in dissipation of eddy kinetic energy in the surface ocean (Müller et al., 2005; Capet et al., 2008b; Barkan et al., 2015; Srinivasan et al., 2023). However, submesoscale dynamics are also known to cascade energy upscale, strengthening mesoscale features (Schubert et al., 2020; Sandery & Sakov, 2017; Qiu et al., 2014). Determining the specifics of the dynamics in this transitional range of 100 m–100 km is essential for quantifying kinetic energy cycles in the ocean (Ferrari & Wunsch, 2009; McWilliams, 2016; Naveira Garabato et al., 2022).

The submesoscale is defined dynamically as the regime where the Rossby number, a non-dimensional parameter defined as $\mathrm{Ro} = U/(fL)$, is order 1 with velocity U, horizontal length scale L, and Coriolis parameter f. While geostrophic dynamics are thought to predominate at the mesoscale and larger, geostrophic balance can begin to break down at the submesoscale. At the larger end of the submesoscale, the surface quasigeostrophy framework presupposes that surface density fronts modify geostrophic balance (Klein & Lapeyre, 2009) while other theoretical results emphasize the role of non-linear advection in submesoscale dynamics (Barkan et al., 2019).

In this work we characterize the transition to submesoscale dynamics at scales smaller than 10 km and provide observational analysis of the kinetic energy cascade that has been hypothesized from models and theory. We observe submesoscale ocean surface velocity using remote sensing from airplanes during the submesoscale ocean dynamics experiment (S-MODE) field campaign (Farrar et al., 2020). We find substantial kinetic energy at the submesoscale, with a kinetic energy spectral slope that is nearly continuous from 100 to 1 km spatial scales. The dynamics that result in the spatial distribution of kinetic energy at the submesoscale are diagnosed through analysis of velocity cross spectra. These reveal that non-linear interactions between balanced and unbalanced dynamics contribute to submesoscale energy and illuminate the dynamics influencing upper-ocean velocity gradient distributions.

2 Methods

2.1 Remote sensing

The observations used in this study were collected by the DoppVis instrument (Lenain et al., 2023), a new sensor that is part of the Modular Aerial Sensing System (MASS; Melville et al., 2016), that infers currents from optical observations of the spatio-temporal evolution, i.e. dispersion relationship, of surface waves. This method infers the depth-resolved Lagrangian current in the upper ocean. Here, we use the depth averaged current over the upper 2 meters. Details about the DoppVis instrument are available in Lenain et al. (2023). The instrument package was installed on a Twin Otter DH-6 aircraft, flying at constant altitude above mean sea level (hereafter, altitude), with a flight profile consisting of repeated reciprocal straight tracks. Consistency between the reciprocal passes is used to validate velocity measurements. Velocity observations are binned to 256 m or 500 m prior to analysis.

Sea surface temperature observations are collected with a Flir SC6700SLS long-wave IR camera (1 m resolution) and Heitronics KT19.85 II infrared thermometer (50 m resolution) (see Melville et al., 2016; Lenain et al., 2023, for details).

Observations from two field campaigns are considered in this study. The first field campaign sampled across a cold filament approximately 70 nautical miles offshore of California, as part of the NASA S-MODE program (Farrar et al., 2020). This region is subsequently referred to as the “filament region” and is the focus of this study. These observations occurred on November 3, 2021 from 18:23 to 23:33 UTC while flying at approximately 500 m altitude and on November 5, 2021 from 22:40 to 23:00 UTC while flying at 940 m altitude (Figure 1A-C).

The higher altitude flight on November 5 enables collection of multiple data points in the cross-swath direction, resulting in a 1.5 km wide swath that is used to compute velocity gradients using central differences. The observations from November 5 are binned at 256 m prior to analysis.

The second field campaign collected observations across two counter-rotating eddies approximately 45 nautical miles offshore of San Diego on May 19, 2021 from 20:56 to 23:26 UTC (Lenain et al., 2023). This region is referred to as the “eddy region”. Observations using a vessel mounted ADCP were collected under the long northwest-to-southeast leg of the DoppVis observations from May 19, 2021 10:00 to May 20, 2021 13:00 UTC.

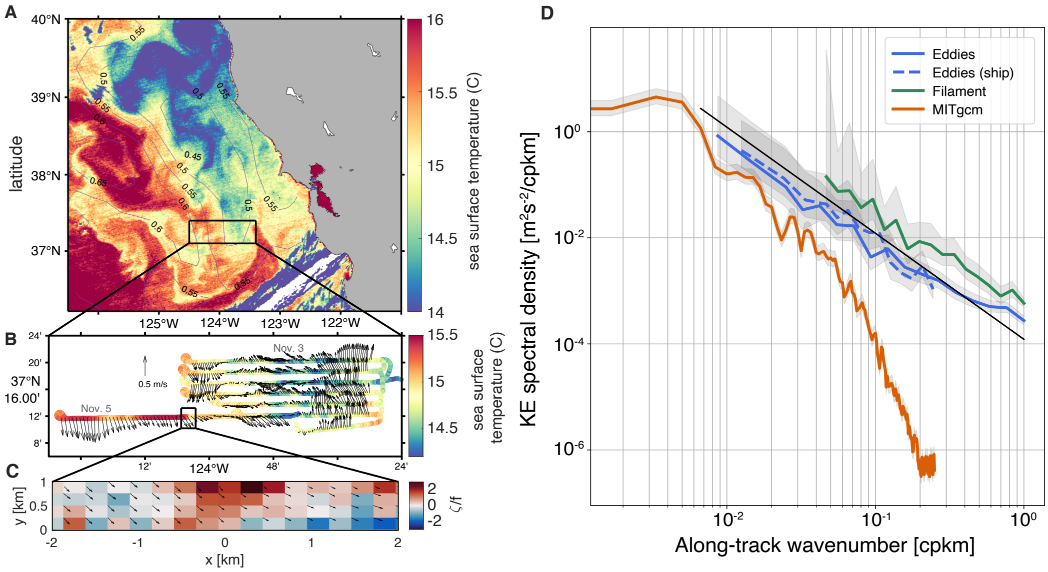

Figure 1. Velocity observations situated in the large-scale context using satellite observations. (A) Satellite (MODIS Aqua) sea surface temperature in the filament region on November 4, 2021 at 21:05Z. Contours show sea surface height from AVISO. (B) DoppVis velocity across the sampled filament (black rectangle in panel A) is shown as vectors with sea surface temperature from the infrared thermometer. Two days of observations are shown, November 3 and November 5. The filament had shifted on November 5. (C) Vorticity computed from DoppVis in the black rectangle in panel B with velocity vectors. This section is shown in Fig. 4A,B. Velocity gradients in Fig. 2 and 4C are computed from the whole transect collected on November 5. (D) Kinetic energy spectral density as a function of along-track wavenumber from a 2 km resolution regional MITgcm model and two observational regions – the eddy region (May 2021) and the filament region (November 2021; panel B) – and two measurement platforms during May 2021 – DoppVis and a ship. The black line shows a k^{-2} spectral slope.

2.2 Spectra

We analyze both the kinetic energy spectrum ($\hat{E}(f)$) and the cross spectrum ($\hat{S}(f)$) with 95% confidence intervals calculated following Bendat and Piersol (2011). Both the kinetic energy spectra and the cross-spectrum between along-track and across-track velocity are computed using Welch's method with Hanning windows.

3 Results

3.1 Kinetic energy spectrum

The multi-scale nature of the flow is quantified using energy spectra, which can also be used to make inferences about the dominant dynamics governing the flow (Callies & Ferrari, 2013). The filament region is more energetic than the eddy region (Figure 1D), with approximately twice the amount of energy at nearly all spatial scales sampled. The kinetic energy spectra of the DoppVis observations have slopes that are approximately k^{-2} (Figure 1D). The observed kinetic energy spectrum crossing the eddies has magnitude and spectral slope similar to that of the spectra from currents (15 m depth) taken with a vessel mounted acoustic Doppler current profiler (ADCP) on a nearby transect on the same day for 5–100 km scales. Differences between the spectra computed from

DoppVis and the ship are within uncertainty but could be due to vertical shear since the DoppVis observations are averages in the upper 2 m. Differences may also be attributable to aliasing in the observations from the ship, which took 30 hours to complete the transect while DoppVis took 50 minutes.

This analysis extends the observations to smaller spatial scales than have been observed previously. Notably, these scales are smaller than those resolved by state-of-the-art global and regional models. As an example, we show the kinetic energy spectrum from a 2 km grid spacing MITgcm regional model of the California current system (Mazloff et al., 2020) (Figure 1D, red line). This model is forced with ERA5 atmospheric state, Hybrid Coordinate Ocean Model + Navy Coupled Ocean Data Assimilation boundary conditions, and both local and remote tides. The effective resolution of this model is 20 km with the velocity spectrum falling off steeply below that scale due to grid scale dissipation. Even at larger scales, both regions are more energetic than the 2 km grid spacing ocean model of the same region (the eddy region is 5 times more energetic). The discrepancy between model and observations at lower wavenumbers is likely caused by an inverse cascade of submesoscale energy energizing surface mesoscale features in ways that are not represented in the model (Lévy et al., 2001; Mahadevan & Tandon, 2006) and by biased observational sampling toward more energetic features. It is important to note that only the larger end of submesoscale dynamics are resolved by 2 km models (Su et al., 2018; Sinha et al., 2022). This is especially important to keep in mind when considering cross-scale energy fluxes that may be modified by dynamics at small spatial scales.

The observed kinetic energy spectral slopes are consistent with previous observations from this region: a comprehensive analysis of surface velocities measured from vessel-mounted ADCPs in the California Current region from 1993–2004 found that the kinetic energy spectral slope in this region is approximately k^{-2} to $k^{-5/3}$ at scales of 10 to 200 km (Chereskin et al., 2019). This is in contrast to the steeper spectral slope (k^{-3}) in more energetic regions such as the Antarctic Circumpolar Current, which implies geostrophic dynamics (Rocha et al., 2016). Modeling studies in the California Current System have found the kinetic energy spectrum to be continuous from the mesoscale to submesoscale, with a slope of approximately k^{-2} (Capet et al., 2008a).

A range of dynamics could result in the observed spectral slope including internal gravity waves (k^{-2}), surface quasigeostrophy ($k^{-5/3}$), and fronts (k^{-2}) (Boyd, 1992; Lapeyre & Klein, 2006). The observations available in this study cannot sufficiently distinguish these spectral slopes, nor can we identify whether the observed slope has transitions in the submesoscale regime from current methods. We therefore rely on further analysis to infer the dynamics in this region.

3.2 Distributions of vorticity, divergence, and strain rate

One of the implications of a kinetic energy spectrum $E(k)$ with a k^{-2} slope is that the velocity derivative spectrum $V(k)$ is flat because the spectra are linked through the relationship $V(k) = k^2E(k)$. The key velocity derivative quantities, divergence ($\delta = u_x + v_y$), vorticity ($\zeta = v_x - u_y$), and strain are related to each other through a system of coupled non-linear ordinary differential equations (c.f. Barkan et al., 2019). The strain is composed of shear strain ($\sigma_s = v_x + u_y$) and normal strain ($\sigma_n = u_x - v_y$).

In the observations that allow for computing gradient across the track, which are only available for one track in the filament case (Figure 1B,C), we find that the vorticity is skewed positive (skewness 0.54, 90% confidence interval [0.49,0.69]), and the divergence is skewed negative (skewness -0.081, 90% confidence interval [-0.17, 0.043]) (Figure 2A,B), consistent with previous (shipboard) observations (Shcherbina et al., 2009; Rudnick, 2001). This skewness can arise from conservation of potential vorticity at fronts. Strain-driven frontogenesis at the sea surface, in the absence of dissipation, results in an infinitely sharp front in finite time with ageostrophic flow that has skewed distributions of divergence (negative) and vorticity (positive) (Hoskins & Bretherton, 1972; Barkan et al., 2019). In addition, the dynamical feedbacks are such that large negative relative

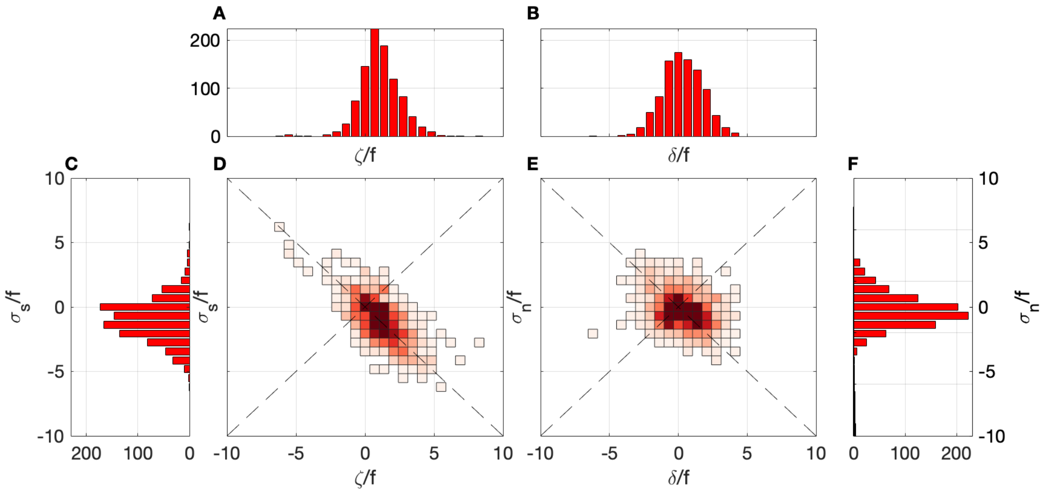

Figure 2. Velocity gradients in the filament observed on October 5 displayed as PDFs of (A) vorticity (ζ), (B) divergence (δ) (C) shear strain (σ_s), and (F) normal strain (σ_n), all normalized by f, along with joint PDFs of vorticity and shear strain (D) and divergence and normal strain (F).

vorticity is typically unstable to symmetric and centrifugal instabilities but positive relative vorticity stabilizes the flow to these instabilities, and therefore a skewed distribution develops (Rudnick, 2001; Buckingham et al., 2016). Compared with anticyclonic fronts, cyclonic fronts also progress more slowly to singularities during frontogenesis, which could result in longer lived cyclonic fronts (Shakespeare, 2016). However, it is notable that strain-driven frontogenesis can suppress the growth of symmetric instability (Thomas, 2012). In boundary layers, negative potential vorticity can arise from frictional and atmospheric forcing, which can trigger symmetric instability.

In the filament observations studied here, vorticity is strongly correlated with shear strain (Figure 2D). This arises not because of direct forcing of vorticity by shear strain but instead because $\sigma_s \approx u_y \approx -\zeta$ in geographic coordinates (x points eastward and y points northward) over much of the sampled domain (but $\zeta \approx v_x$ at the front shown in Figure 4). Shear strain and vorticity are correlated due to the relative stability of cyclonic vorticity at straight fronts (Buckingham et al., 2021). This provides an explanation for the strain–vorticity relationship that has been observed in high-resolution simulations (Balwada et al., 2021). However, there is not a strong correlation between divergence and normal strain ($\sigma_n = u_x - v_y$); while non-zero vorticity can be maintained in an adiabatic system in the absence of divergence and vertical motion, a similar balance does not exist for divergence (Figure 2E).

3.3 Non-linear interactions

At the submesoscale (Ro$\sim \mathcal{O}(1)$), the flow becomes more fully three dimensional (velocity divergence $\delta \sim U/L$). A key dynamical transitions at the submesoscale is that temporal changes in velocity gradient quantities (vorticity, divergence, and strain) are coupled such that non-linear feedbacks become important (Barkan et al., 2019). For example, the rate of change of vorticity in an adiabatic system is

$$\frac{D\zeta}{Dt} = -f\delta - \delta\zeta - w_x v_z + w_y u_z. \tag{1}$$

Only the first term, which does not involve a feedback, is present in a quasigeostrophic system. In addition, at the submesoscale the inertial term in the equations of motion ($u\cdot$

$\nabla u \sim U^2/L$) is of the same order as the Coriolis term ($uf \sim Uf$), facilitating cross-scale kinetic energy transfers.

3.3.1 Interactions between rotational and divergent flow

The approximately k^{-2} spectral slope in both the filament and eddy regions is informative but inconclusive about the about the dominant dynamics operating in these regions. The nearly uniform slope across the observed spatial scales leaves open questions about the scales at which a transition to submesoscale dynamics may occur.

The submesoscale feedback between vorticity and divergence (equation 1) results in a correlation between the geostrophically balanced rotational (streamfunction) flow and the divergent (potential) component of the velocity. We diagnose when the streamfunction and potential become correlated using the cross spectrum between the along-track (u) and cross track (v) velocity components.

When the streamfunction and potential are uncorrelated, as is typically true at the mesoscale and larger, the cross spectrum of the u and v velocity components is a superposition of the spectra of the streamfunction and velocity potential. In this case, since spectra are real, the cross spectrum is real (Bühler et al., 2017). This is a key assumption of the 'wave–vortex' decomposition introduced by Bühler et al. (2014). However, when the rotational and divergent flow components interact, the cross spectrum between the along-track and across-track velocity ($\hat{S}_{uv}$) is complex. We are therefore able to diagnose the spatial scale where a shift to submesoscale dynamics occurs as the scale at which the cross spectrum becomes complex. The cross spectral phase should only be interpreted in this manner if the coherence, which is the normalized cross spectrum between the along-track and across track velocity, is significant. Coherence is related to flow anisotropy because $\mathbb{E}(uv) = 0$ for isotropic flows, but it is not a quantitative measure of anisotropy. For isotropic flows, the Bühler et al. (2014) decomposition may be applied even if the streamfunction and potential are correlated (Callies et al., 2016).

The squared coherence has contrasting dependence on spatial scale in the two regions studied here (Figure 3A). In the eddy region (blue lines in Figure 3), the squared coherence is large at the largest spatial scales sampled (∼100 km) and decreases steadily to 10 km scales after which it flattens out, but remains significantly different from zero. In the filament region (green lines), the squared coherence is also large at the largest spatial scales sampled (∼10 km), decreases at scales larger than 6 km, and then increases again toward the smallest spatial scales sampled (∼1 km). Fronts and filaments are expected to be anisotropic at the scale of the feature, as is observed. In all observations considered here, the coherence is large enough to be statistically significant, allowing for analysis of the cross-spectral phase. The only exception is in the eddy region between 0.1 and 0.6 cpkm where the coherence falls below the significance threshold, suggesting that the eddy region is relatively isotropic at mesoscale.

The cross-spectral phase summarizes the relationship between the real and imaginary parts of the cross spectrum. When the cross spectrum is purely real, the phase is 0° or 180°; when it is purely imaginary, the phase is ±90°. We find abrupt transitions at a scale slightly smaller than 10 km in the eddy region and 6 km in the filament region, where the imaginary part of the cross spectrum becomes larger than the real part (Figure 3B). This 6 km spatial scale is the same scale where the coherence increases in the filament region (suggesting increased anisotropy), providing consistent evidence of a change to increasingly non-linear frontal dynamics at these scales. By contrast, in a surface quasigeostrophic model, which neglects ageostrophic advection, the real part of the cross spectrum dominates at all spatial scales (Figure S3). During the eddy observations, the mixed-layer depth was 40–55 m with some regions as shallow as 15 m. In contrast, for the filament observations, the mixed-layer depth was approximately 35 m or shallower and the stratification was approximately 3×10^{-5} s^{-2}. Therefore, the mixed-layer deformation radius was 2–4 km for these locations, implying that the fastest growing baroclinic mode is around 8–24 km (Dong et al., 2020). Thus, the transition to non-

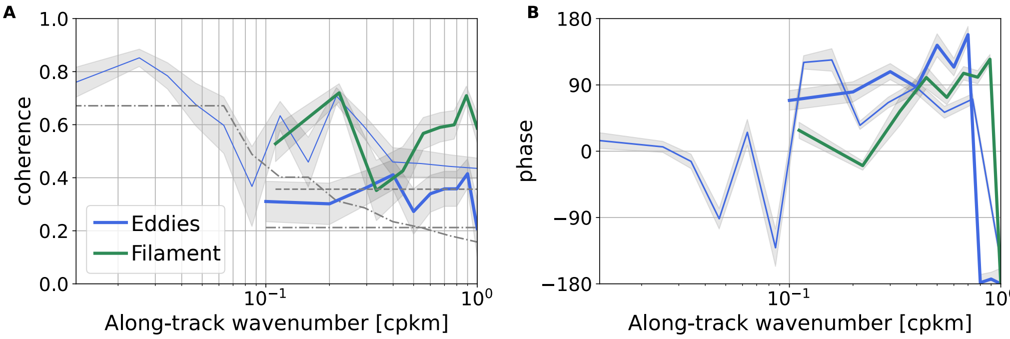

Figure 3. Flow anisotropy and non-linearity revealed by analysis of velocity cross spectrum. (A) Squared coherence as a function of wavenumber. The gray lines show the significance threshold (dashed and dot dash show filament and eddies, respectively) and the shading shows standard deviation. (B) Cross-spectrum phase. The thin lines in show the squared coherence computed from two long transects in the eddy region with 80 km windows while the thick lines show the squared coherence computed from the two long sections and four shorter sections (which crossed the eddy nearly perpendicularly, SI Fig. S1) using 10 km windows.

linear ageostrophic dynamics observed here occurs in the approximate range of the scale of mixed-layer baroclinic instability.

There are a number of mechanisms that could be responsible for the interaction between rotational and divergent velocity. In the filament case, the interaction of the ageostrophic frontal divergence and larger scale geostrophic flow is likely the dominant mechanism. Here we find that the shift to a mostly imaginary cross spectrum is localized in the regions of largest velocity gradient (Figure S4). The eddy case likely encompasses a larger range of dynamics, including near-inertial oscillations modified by the vorticity of the observed features, frontal dynamics, and submesoscale vortices.

3.3.2 Spectral energy transfers

The distribution of kinetic energy across spatial scales reflects dynamics that are local in wavenumber, but importantly also reflects energy transfers across scales. At the submesoscale, major open questions remain regarding the direction of the energy cascade, the mechanisms that lead to a forward energy, and the rate of the forward energy cascade (Müller et al., 2005; McWilliams, 2016). Forward energy flux precedes dissipation at small spatial scales by turbulent processes.

The energy transfer across scales can be quantified using coarse graining (Germano, 1992; Eyink, 2005; Aluie et al., 2018). The kinetic energy flux is defined here as

$$\Pi = -(\tau_{uv}(u_y + v_x) + \tau_{uu}u_x + \tau_{vv}v_y) \tag{2}$$

where $\tau_{ab} = \overline{ab} - \bar{a}\,\bar{b}$ and $\bar{\cdot}$ is a top hat filter. Positive (negative) values indicate a flux of energy toward smaller (larger) spatial scales. We use velocity observed on a 256 m grid and a top hat filter with a scale of 1 km to compute an instantaneous energy flux across the observed transect. Error is estimated using a bootstrapped confidence intervals and a velocity error of 0.05 m s^{-1} (Lenain et al., 2023).

In the frontal regions in this flow, there is a strong forward energy flux localized in a 1 km region at the frontal outcrop where there is also a peak in frontogenesis (Figure 4A,B). The energy flux to smaller spatial scales is driven by the first term in equation 2 (Figure S5). This term involves the shear strain multiplied by the scale-dependent

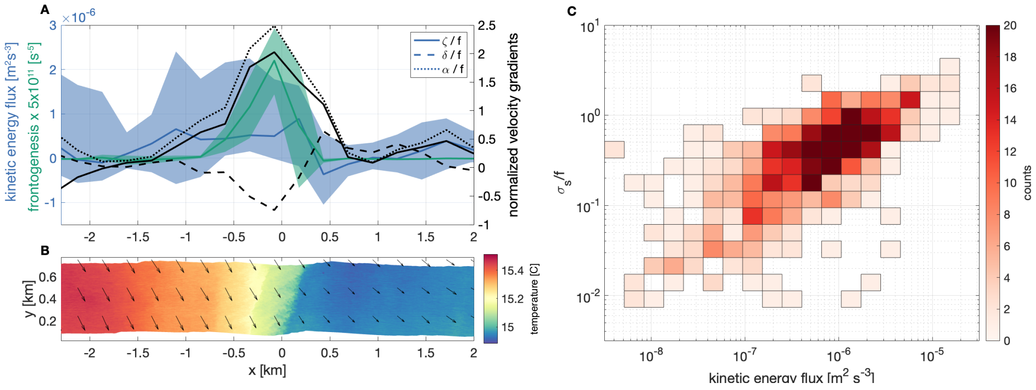

Figure 4. Spatial distribution of kinetic energy flux and frontogenesis. (A) Kinetic energy flux across 1 km and buoyancy frontogenesis (shading shows the bootstrapped 95% confidence interval) and vorticity, divergence, and strain ($\alpha = \sqrt{\sigma_n^2 + \sigma_s^2}$) at one of the fronts on the sampled transect. (B) Sea surface temperature measured from long wave infrared. Velocity is shown with vectors. (C) Joint probability density function of kinetic energy flux from the whole transect and shear strain.

covariance between the along track and cross track velocity. In fact, over the entire 60 km section, there is a strong correlation between the shear strain and the kinetic energy flux (Figure 4C).

The influence of the shear strain on the kinetic energy flux is modulated by the covariance between the u and v velocity components (or, equivalently, the anistropy of the flow), which becomes large below scales of 6 km in this filament region (Figure 3A). Barotropic shear instabilities extract kinetic energy from sheared mean flows when smaller scale features lean into the shear, resulting in a forward energy cascade.

The observed kinetic energy flux is patchy (Figure 4C), with the largest flux concentrated in small spatial scales even within the 60 km filament region observed here. Within the larger filament region (the 60 km sampling region), the kinetic energy flux varies over three orders of magnitude (Figure 4C). The typical kinetic energy flux across 1 km in the filament region is $\mathcal{O}(10^{-6}\ \mathrm{m^2 s^{-3}})$. This rate is about an order of magnitude larger than the kinetic energy flux obtained from mooring based observations using a filter scale of 5 days (Naveira Garabato et al., 2022) and in a modeling study at 500 m spatial resolution (Srinivasan et al., 2023). Given that we present direct observations of the kinetic energy flux terms, this suggests that the magnitude of instantaneous kinetic energy flux has been underestimated by previous modeling and observational work.

4 Discussion and conclusion

The airborne observations presented here reveal a transition to non-linear submesoscale dynamics at scales of 6–10 km with implications for kinetic energy flux. The synoptic sampling from submesoscale to mesoscale allows us to extend an observational kinetic energy spectrum to scales below 1 km. Dense filaments such as the one observed here have an important role in the energetics of upwelling systems with submesoscale dynamics influencing the fate of upwelled waters.

We demonstrate that although there is not a clear change in the kinetic energy spectral slope, there is a transition in the dynamics to non-linear interactions that characterize submesoscales at scales of $\mathcal{O}(1\ \mathrm{km})$. In particular, this transition is characterized by the interaction between divergent and rotational velocity components. This transition would not occur with surface quasigeostrophic dynamics and we attribute it instead to a dominance of ageostrophic dynamics in the observations.

The observed transition to non-linearity has important implications for observations of ocean velocity from remote sensing. For example, the SWOT mission aims to infer mesoscale to submesoscale velocities through observation of sea surface height. These velocities are computed through geostrophic balance, which only accounts for the rotational component of the flow. Not only do we find that a significant amount of the kinetic energy is likely in the divergent component of the flow at scales below 10 km in this region — and potentially at larger scales in more energetic regions (Callies et al., 2015) — but also that the rotational and divergent flows interact such that filtering of the divergent processes (e.g. waves) will not result in recovering the rotational component of the flow.

These observations are also the first direct observations of *snapshots* of kinetic energy flux and frontogenesis in the ocean. This allows us to investigate the relationships between the kinetic energy flux and hydrographic features. We find that kinetic energy flux is patchy but can be large (10^{-6} m^{2}s^{-3}) at submesoscale fronts. The patchiness of kinetic energy flux has important implications for resolving the dynamics that contribute to an energy cascade. Due to the difficulty resolving scales ranging from mesoscale straining to turbulent dissipation in models, these observations — where that challenge is observationally addressed using a novel remote sensing platform — are particularly valuable. These aircraft measurements provide a precursor to what might be possible from future satellite-based radar snapshots from platforms such as Harmony and Seastar (Gommenginger et al., 2019; López-Dekker et al., 2019). In these observations, kinetic energy is transferred both downscale and upscale from 1 km.

Recent modeling work has suggested that resolving frontogenesis is essential to accurate representation of submesoscale kinetic energy transfers (Naveira Garabato et al., 2022; Srinivasan et al., 2023). The observations analyzed here demonstrate a large forward energy transfer localized at fronts, although not exclusively during active large-scale frontogenesis. Recent work in the Gulf of Mexico, another region with an active submesoscale, has hinted that a forward cascade of kinetic energy occurs at scales of 500 m–5 km (Balwada et al., 2022) in observations (with smaller scales during the summer) and at scales of 5 km in models (Srinivasan et al., 2023).

The modeling study of Sullivan and McWilliams (2018), which simulated a dense filament, also found an important role for the horizontal Reynolds stress term ($u'v'v_x$) during the frontal arrest phase of a dense filament, which is consistent with our observation that the shear strain term dominated kinetic energy flux. This relationship may arise from certain aspects of the feature studied here and may not generalize to all fronts. For example, Srinivasan et al. (2023) analyzed kinetic energy fluxes in 500 m and 2 km resolution ocean models, which resolve dynamics at larger scales than those that are the focus of our study. They find an equipartition between strain-driven and convergence-driven forward energy cascade at submesoscale scales (Srinivasan et al., 2023). While we observe that the forward energy transfer is strain-driven in our observations, it is important to note that we have only one snapshot of a filament that appears to be partially restratifying, so this does not invalidate the role of convergence in forward energy flux.

These results suggest an out-sized role for fronts and filaments as hotspots of surface kinetic energy flux. Barotropic energy transfer is enabled by interactions between the rotational and divergent components of the flow field at submesoscale fronts. Fronts are spatially inhomogeneously distributed in the ocean and vary seasonally (Drushka et al., 2019; Mauzole et al., 2020), but the distributions of fronts are distinct from the distributions of mesoscale kinetic energy (Busecke & Abernathey, 2019). Surface kinetic energy dissipation may similarly vary substantially in space and time, but understanding how it varies relies on increased mechanistic understanding of the energetics of submesoscale features. Disentangling these would require more observations to establish the effect of particular submesoscale features on the regional statistics.

Acknowledgments

We would like to thank Nick Statom for data collection and Alex Andriatis for ship observations. We would like to acknowledge Matthew Mazloff, Peter Franks, Oliver Buhler, Roy Barkan, Jacob Wenegrat, and the S-MODE science team, and particularly J. Thomas Farrar, for discussions about this work and Dhruv Balwada, Han Wang, and an anonymous reviewer for constructive comments on the manuscript. This work was funded by a Scripps Institutional Postdoctoral fellowship and by the Physical Oceanography programs at ONR (Grant N00014-19-1-2635), and NASA (Grants 80NSSC19K1688, 80NSSC20K1136, and 80NSSC21K1822).

Open research

All presented data are available at UCSD Library Digital Collection, https://doi.org/10.6075/J0F76CRK.

References

Aluie, H., Hecht, M., & Vallis, G. K. (2018, February). Mapping the Energy Cascade in the North Atlantic Ocean: The Coarse-Graining Approach. *Journal of Physical Oceanography*, *48*(2), 225–244. doi: 10.1175/JPO-D-17-0100.1

Balwada, D., Xiao, Q., Smith, S., Abernathey, R., & Gray, A. R. (2021, September). Vertical Fluxes Conditioned on Vorticity and Strain Reveal Submesoscale Ventilation. *Journal of Physical Oceanography*, *51*(9), 2883–2901. doi: 10.1175/JPO-D-21-0016.1

Balwada, D., Xie, J.-H., Marino, R., & Feraco, F. (2022, October). Direct observational evidence of an oceanic dual kinetic energy cascade and its seasonality. *Science Advances*, *8*(41), eabq2566. doi: 10.1126/sciadv.abq2566

Barkan, R., Molemaker, M. J., Srinivasan, K., McWilliams, J. C., & D'Asaro, E. A. (2019). The role of horizontal divergence in submesoscale frontogenesis. *Journal of Physical Oceanography*, *49*(6), 1593–1618.

Barkan, R., Winters, K. B., & Smith, S. G. L. (2015, January). Energy Cascades and Loss of Balance in a Reentrant Channel Forced by Wind Stress and Buoyancy Fluxes. *Journal of Physical Oceanography*, *45*(1), 272–293. doi: 10.1175/JPO-D-14-0068.1

Bendat, J. S., & Piersol, A. G. (2011). *Random Data: Analysis and Measurement Procedures*. John Wiley & Sons.

Boyd, J. P. (1992, January). The Energy Spectrum of Fronts: Time Evolution of Shocks in Burgers Equation. *Journal of the Atmospheric Sciences*, *49*(2), 128–139. doi: 10.1175/1520-0469(1992)049⟨0128:TESOFT⟩2.0.CO;2

Buckingham, C. E., Gula, J., & Carton, X. (2021). The role of curvature in modifying frontal instabilities. Part I: Review of theory and presentation of a nondimensional instability criterion. *Journal of Physical Oceanography*, *51*(2), 299–315.

Buckingham, C. E., Naveira Garabato, A. C., Thompson, A. F., Brannigan, L., Lazar, A., Marshall, D. P., ... Belcher, S. E. (2016). Seasonality of submesoscale flows in the ocean surface boundary layer. *Geophysical Research Letters*, *43*(5), 2118–2126. doi: 10.1002/2016GL068009

Busecke, J. J. M., & Abernathey, R. P. (2019, January). Ocean mesoscale mixing linked to climate variability. *Science Advances*, *5*(1), eaav5014. doi: 10.1126/sciadv.aav5014

Bühler, O., Callies, J., & Ferrari, R. (2014, October). Wave–vortex decomposition of one-dimensional ship-track data. *Journal of Fluid Mechanics*, *756*, 1007–1026. doi: 10.1017/jfm.2014.488

Bühler, O., Kuang, M., & Tabak, E. G. (2017, March). Anisotropic Helmholtz and wave–vortex decomposition of one-dimensional spectra. *Journal of Fluid Mechanics*, *815*, 361–387. doi: 10.1017/jfm.2017.57

Callies, J., & Ferrari, R. (2013). Interpreting energy and tracer spectra of upper-ocean turbulence in the submesoscale range (1–200 km). *Journal of Physical Oceanography*, *43*(11), 2456–2474.

Callies, J., Ferrari, R., Klymak, J. M., & Gula, J. (2015). Seasonality in submesoscale turbulence. *Nature communications*, *6*(1), 1–8.

Callies, J., Flierl, G., Ferrari, R., & Fox-Kemper, B. (2016). The role of mixed-layer instabilities in submesoscale turbulence. *Journal of Fluid Mechanics*, *788*, 5–41.

Capet, X., McWilliams, J. C., Molemaker, M. J., & Shchepetkin, A. (2008a). Mesoscale to submesoscale transition in the California Current System. Part I: Flow structure, eddy flux, and observational tests. *Journal of Physical Oceanography*, *38*(1), 29–43.

Capet, X., McWilliams, J. C., Molemaker, M. J., & Shchepetkin, A. F. (2008b, October). Mesoscale to Submesoscale Transition in the California Current System. Part III: Energy Balance and Flux. *Journal of Physical Oceanography*, *38*(10), 2256–2269. doi: 10.1175/2008JPO3810.1

Chereskin, T. K., Rocha, C. B., Gille, S. T., Menemenlis, D., & Passaro, M. (2019). Characterizing the Transition From Balanced to Unbalanced Motions in the Southern California Current. *Journal of Geophysical Research: Oceans*, *124*(3), 2088–2109. doi: 10.1029/2018JC014583

Dong, J., Fox-Kemper, B., Zhang, H., & Dong, C. (2020, September). The Scale of Submesoscale Baroclinic Instability Globally. *Journal of Physical Oceanography*, *50*(9), 2649–2667. doi: 10.1175/JPO-D-20-0043.1

Drushka, K., Asher, W. E., Sprintall, J., Gille, S. T., & Hoang, C. (2019, July). Global Patterns of Submesoscale Surface Salinity Variability. *Journal of Physical Oceanography*, *49*(7), 1669–1685. doi: 10.1175/JPO-D-19-0018.1

Eyink, G. L. (2005, July). Locality of turbulent cascades. *Physica D: Nonlinear Phenomena*, *207*(1), 91–116. doi: 10.1016/j.physd.2005.05.018

Farrar, J. T., D'Asaro, E., Rodriguez, E., Shcherbina, A., Czech, E., Matthias, P., ... Jenkins, R. (2020, September). S-MODE: The Sub-Mesoscale Ocean Dynamics Experiment. In *IGARSS 2020 - 2020 IEEE International Geoscience and Remote Sensing Symposium* (pp. 3533–3536). doi: 10.1109/IGARSS39084.2020.9323112

Ferrari, R., & Wunsch, C. (2009). Ocean Circulation Kinetic Energy: Reservoirs, Sources, and Sinks. *Annual Review of Fluid Mechanics*, *41*(1), 253–282. doi: 10.1146/annurev.fluid.40.111406.102139

Freilich, M., Flierl, G., & Mahadevan, A. (2022). Diversity of Growth Rates Maximizes Phytoplankton Productivity in an Eddying Ocean. *Geophysical Research Letters*, *49*(3), e2021GL096180. doi: 10.1029/2021GL096180

Germano, M. (1992, May). Turbulence: the filtering approach. *Journal of Fluid Mechanics*, *238*, 325–336. doi: 10.1017/S0022112092001733

Gommenginger, C., Chapron, B., Hogg, A., Buckingham, C., Fox-Kemper, B., Eriksson, L., ... Burbidge, G. (2019). SEASTAR: A Mission to Study Ocean Submesoscale Dynamics and Small-Scale Atmosphere-Ocean Processes in Coastal, Shelf and Polar Seas. *Frontiers in Marine Science*, *6*.

Hoskins, B. J., & Bretherton, F. P. (1972). Atmospheric frontogenesis models: Mathematical formulation and solution. *Journal of the Atmospheric Sciences*, *29*(1), 11–37.

Klein, P., & Lapeyre, G. (2009). The Oceanic Vertical Pump Induced by Mesoscale and Submesoscale Turbulence. *Annual Review of Marine Science*, *1*(1), 351–375.

Lapeyre, G., & Klein, P. (2006). Impact of the small-scale elongated filaments on the oceanic vertical pump. *Journal of Marine Research*, *64*(6), 835–851.

Lenain, L., Smeltzer, B. K., Pizzo, N., Freilich, M., Colosi, L., Ellingsen, S., ... Statom, N. (2023). Airborne observations of surface winds, waves and currents from meso to submesoscales. *submitted*.

Lévy, M., Klein, P., & Treguier, A.-M. (2001). Impact of sub-mesoscale physics on production and subduction of phytoplankton in an oligotrophic regime. *Journal of Marine Research*, *59*(4), 535–565.

López-Dekker, P., Rott, H., Prats-Iraola, P., Chapron, B., Scipal, K., & Witte, E. D. (2019, July). Harmony: an Earth Explorer 10 Mission Candidate to Observe Land, Ice, and Ocean Surface Dynamics. In *IGARSS 2019 - 2019 IEEE International Geoscience and Remote Sensing Symposium* (pp. 8381–8384). doi: 10.1109/IGARSS.2019.8897983

Mahadevan, A. (2016). The impact of submesoscale physics on primary productivity of plankton. *Annual Review of Marine Science*, *8*, 161–184.

Mahadevan, A., & Tandon, A. (2006). An analysis of mechanisms for submesoscale vertical motion at ocean fronts. *Ocean Modelling*, *14*(3-4), 241–256.

Mauzole, Y. L., Torres, H. S., & Fu, L.-L. (2020). Patterns and Dynamics of SST Fronts in the California Current System. *Journal of Geophysical Research: Oceans*, *125*(2), e2019JC015499. doi: 10.1029/2019JC015499

Mazloff, M. R., Cornuelle, B., Gille, S. T., & Wang, J. (2020). The Importance of Remote Forcing for Regional Modeling of Internal Waves. *Journal of Geophysical Research: Oceans*, *125*(2), e2019JC015623. doi: 10.1029/2019JC015623

McWilliams, J. C. (2016). Submesoscale currents in the ocean. *Proceedings of the Royal Society A: Mathematical, Physical and Engineering Sciences*, *472*(2189), 20160117.

Melville, W. K., Lenain, L., Cayan, D. R., Kahru, M., Kleissl, J. P., Linden, P. F., & Statom, N. M. (2016, June). The Modular Aerial Sensing System. *Journal of Atmospheric and Oceanic Technology*, *33*(6), 1169–1184. doi: 10.1175/JTECH-D-15-0067.1

Müller, P., McWilliams, J. C., & Molemaker, M. J. (2005). Routes to dissipation in the ocean: The 2D/3D turbulence conundrum. In *Marine turbulence: theories, observations and models* (pp. 397–405). Cambridge, Uk: Cambridge University Press.

Naveira Garabato, A. C., Yu, X., Callies, J., Barkan, R., Polzin, K. L., Frajka-Williams, E. E., … Griffies, S. M. (2022, January). Kinetic Energy Transfers between Mesoscale and Submesoscale Motions in the Open Ocean's Upper Layers. *Journal of Physical Oceanography*, *52*(1), 75–97. doi: 10.1175/JPO-D-21-0099.1

Qiu, B., Chen, S., Klein, P., Sasaki, H., & Sasai, Y. (2014). Seasonal mesoscale and submesoscale eddy variability along the North Pacific Subtropical Countercurrent. *Journal of Physical Oceanography*, *44*(12), 3079–3098.

Rocha, C. B., Chereskin, T. K., Gille, S. T., & Menemenlis, D. (2016). Mesoscale to submesoscale wavenumber spectra in Drake Passage. *Journal of Physical Oceanography*, *46*(2), 601–620.

Rudnick, D. L. (2001). On the skewness of vorticity in the upper ocean. *Geophysical Research Letters*, *28*(10), 2045–2048. doi: 10.1029/2000GL012265

Sandery, P. A., & Sakov, P. (2017, November). Ocean forecasting of mesoscale features can deteriorate by increasing model resolution towards the submesoscale. *Nature Communications*, *8*(1), 1566. doi: 10.1038/s41467-017-01595-0

Schubert, R., Gula, J., Greatbatch, R. J., Baschek, B., & Biastoch, A. (2020, September). The Submesoscale Kinetic Energy Cascade: Mesoscale Absorption of Submesoscale Mixed Layer Eddies and Frontal Downscale Fluxes. *Journal of Physical Oceanography*, *50*(9), 2573–2589. doi: 10.1175/JPO-D-19-0311.1

Shakespeare, C. J. (2016, October). Curved Density Fronts: Cyclogeostrophic Adjustment and Frontogenesis. *Journal of Physical Oceanography*, *46*(10), 3193–3207. doi: 10.1175/JPO-D-16-0137.1

Shcherbina, A. Y., Gregg, M. C., Alford, M. H., & Harcourt, R. R. (2009, November). Characterizing Thermohaline Intrusions in the North Pacific Subtropical

Frontal Zone. *Journal of Physical Oceanography*, *39*(11), 2735–2756. doi: 10.1175/2009JPO4190.1

Sinha, A., Callies, J., & Menemenlis, D. (2022, December). Do Submesoscales Affect the Large-Scale Structure of the Upper Ocean? *Journal of Physical Oceanography*, *-1*(aop). doi: 10.1175/JPO-D-22-0129.1

Srinivasan, K., Barkan, R., & McWilliams, J. C. (2023). A Forward Energy Flux at Submesoscales Driven by Frontogenesis. *Journal of Physical Oceanography*, *53*(1), 287–305. doi: 10.1175/JPO-D-22-0001.1

Strobach, E., Klein, P., Molod, A., Fahad, A. A., Trayanov, A., Menemenlis, D., & Torres, H. (2022). Local Air-Sea Interactions at Ocean Mesoscale and Submesoscale in a Western Boundary Current. *Geophysical Research Letters*, *49*(7), e2021GL097003. doi: 10.1029/2021GL097003

Su, Z., Wang, J., Klein, P., Thompson, A. F., & Menemenlis, D. (2018). Ocean submesoscales as a key component of the global heat budget. *Nature communications*, *9*(1), 775.

Sullivan, P. P., & McWilliams, J. C. (2018, February). Frontogenesis and frontal arrest of a dense filament in the oceanic surface boundary layer. *Journal of Fluid Mechanics*, *837*, 341–380. doi: 10.1017/jfm.2017.833

Thomas, L. N. (2012). On the effects of frontogenetic strain on symmetric instability and inertia–gravity waves. *Journal of Fluid Mechanics*, *711*, 620–640.

Supporting Information for "Non-linear processes characterize the transition to submesoscale dynamics in observations of a dense filament"

Mara Freilich[1], Luc Lenain[1], Sarah T. Gille[1]

[1]Scripps Institution of Oceanography

Contents of this file

1. Definitions

The velocity components can be written in terms of the sum of the velocity streamfunction (ψ) and velocity potential (ϕ)

$$u = \frac{\partial \phi}{\partial x} - \frac{\partial \psi}{\partial y} \tag{1}$$

$$v = \frac{\partial \phi}{\partial y} + \frac{\partial \psi}{\partial x}. \tag{2}$$

The velocity potential is divergent while the streamfunction is rotational.

2. Cross spectrum, coherence, and phase

The cross spectrum ($\hat{S}(f)$) is defined as

$$\hat{S}_{uv}(f) = \frac{\langle \hat{u}^* \hat{v} \rangle}{T}, \tag{3}$$

where $\hat{u}$ is the Fourier transform of the u velocity, and * indicates the complex conjugate (Bendat & Piersol, 2011). The angle brackets indicate averages over ν realizations. u is the along-track velocity and v is the cross-track velocity. The squared coherence is given by

$$\gamma^2_{uv}(f) = \frac{|\hat{S}_{uv}(f)|^2}{\hat{S}_u(f)\hat{S}_v(f)}. \tag{4}$$

$\hat{S}(f) = \hat{C}(f) + i\hat{Q}(f)$ is complex. The phase is given by

$$\tan(\phi_{uv}(f)) = \left(\frac{-\hat{Q}(f)}{\hat{C}(f)} \right). \tag{5}$$

The 95% percent confidence interval of the kinetic energy spectrum is estimated using a standard method by assuming that the ratio of estimated to true spectrum has a χ^2 distribution with expectation ν where ν is the number of segments. The significance of the estimated coherence is assessed using two methods. The 95% significance level is computed as $\sqrt{1-\alpha^{1/(\nu-1)}}$ where $\alpha = 0.05$. The standard deviation of the coherence is calculated as

$$std_{\gamma^2_{uv}} = \frac{\sqrt{2}(1-\gamma^2_{uv})}{|\gamma_{uv}|\sqrt{2\nu}} \tag{6}$$

The standard error of the phase spectrum is calculated as

$$std_{\phi_{uv}} = \frac{\sqrt{1-\gamma^2_{uv}}}{|\gamma_{uv}|\sqrt{2\nu}} \tag{7}$$

3. Surface quasigeostrophic model

A surface quasigeostrophic model (SQG) is used to validate the dynamical interpretation of the cross spectrum as representing contributions from ageostrophic advection. The surface quasigeostrophic model describes a flow field where the interior potential vorticity is zero and the full 3D dynamics are described by the 2D surface flow field. This is a suitable null model for this analysis because it is the simplest model that includes surface fronts but not ageostrophic advection. In this model, the interior potential vorticity is zero

$$\nabla^2\psi + \frac{\partial}{\partial z}\left(\frac{f_0^2}{N_0^2}\frac{\partial \psi}{\partial z}\right) = 0, \tag{8}$$

where ψ is a streamfunction, f_0 is the Coriolis frequency, and N_0 is the buoyancy frequency. f_0 and N_0 are both constant. At depth (as $z \to -\infty$), $\psi = 0$. Surface density gradients are advected by and feedback on the streamfunction ψ

$$\frac{\partial b}{\partial t} + J(\psi, b) = 0. \tag{9}$$

The surface buoyancy gradients are related to the streamfunction through the hydrostatic relationship $b = \psi_z$. We can solve equation 8 for the streamfunction in Fourier space and obtain

$$\hat{\psi} = \frac{f_0}{N_0}\frac{1}{\kappa}\hat{b} \tag{10}$$

We initialize PyQG (Abernathey et al., 2022), a Python implementation of a surface quasigeostrophic model with two counter-rotating eddies. These eddies evolve to form filaments, but the net kinetic energy flux of the resolved dynamics is always upscale (Capet et al., 2008). A cross spectrum of the u and v velocity components in this model shows that the cross spectrum is mostly real, particularly at the smallest wavenumbers, in contrast to the observed patterns (Figure S3).

4. Vertical kinetic energy flux terms

While typically only the horizontal terms are considered in spectral kinetic energy fluxes (Aluie et al., 2018; Balwada et al., 2022; Srinivasan et al., 2023), these observations allow us to diagnose kinetic energy fluxes that are associated with the vertical shear. The full expression for the kinetic energy flux is

$$\Pi_a = -\underbrace{\left(\tau_{uv}(u_y + v_x) + \tau_{uu}u_x + \tau_{vv}v_y\right)}_{\Pi_h} - \underbrace{\left(\tau_{uw}u_z + \tau_{vw}v_z\right)}_{\Pi_v} - \underbrace{\left(\tau_{ww}w_z\right)}_{\Pi_{ww}} \tag{11}$$

The first term Π_h is shown in the main text. The second term, Π_v, is associated with baroclinicity of the flow. Here we diagnose this term using the velocity and sea surface temperature observations. The third term, Π_w, cannot be diagnosed with the available observations, but it is expected to be small. We compute Π_v by calculating the vertical velocity as $w = \delta \times h$ where δ is the surface divergence and h is the integration depth. Here, the integration depth is 1 meter, which is the approximate depth over which the surface velocity observations have been averaged (Lenain et al., 2023). The shear terms are computed from thermal wind balance. However, given that only sea surface temperature observations are available, we convert sea surface temperature to density using thermosalinograph observations from a ship that was nearby. The observed fronts are partially salinity compensated so the density is computed from temperature using a relationship within the observed temperature range. We find that Π_v peaks at the front, where δ is large, and is negative while Π_h is positive (Figure S6). However, Π_v is still at least an order of magnitude smaller than Π_h.

References

Abernathey, R., rochanotes, Ross, A., Jansen, M., Li, Z., Poulin, F. J., ... Tobias (2022). *pyqg/pyqg: v0.7.2.* Zenodo. Retrieved 2023-03-17, from https://zenodo.org/record/6563667 doi: 10.5281/zenodo.6563667

Aluie, H., Hecht, M., & Vallis, G. K. (2018). Mapping the Energy Cascade in the North Atlantic Ocean: The Coarse-Graining Approach. *Journal of Physical Oceanography*, *48*(2), 225–244. Retrieved 2022-08-23, from https://journals.ametsoc.org/view/journals/phoc/48/2/jpo-d-17-0100.1.xml (Publisher: American Meteorological Society Section: Journal of Physical Oceanography) doi: 10.1175/JPO-D-17-0100.1

Balwada, D., Xie, J.-H., Marino, R., & Feraco, F. (2022). Direct observational evidence of an oceanic dual kinetic energy cascade and its seasonality. *Science Advances*, *8*(41), eabq2566. Retrieved 2023-03-20, from https://www.science.org/doi/full/10.1126/sciadv.abq2566 (Publisher: American Association for the Advancement of Science) doi: 10.1126/sciadv.abq2566

Bendat, J. S., & Piersol, A. G. (2011). *Random Data: Analysis and Measurement Procedures.* John Wiley & Sons.

Capet, X., Klein, P., Hua, B. L., Lapeyre, G., & Mcwilliams, J. C. (2008). Surface kinetic energy transfer in surface quasi-geostrophic flows. *Journal of Fluid Mechanics*, *604*, 165–174. Retrieved 2023-03-17, from https://www.cambridge.org/core/journals/journal-of-fluid-mechanics/article/surface-kinetic-energy-transfer-in-surface-quasigeostrophic-flows/

5AEDA38EF14C0C33AA1AC073BCF51087 (Publisher: Cambridge University Press) doi: 10.1017/S0022112008001110

Lenain, L., Smeltzer, B. K., Pizzo, N., Freilich, M., Colosi, L., Ellingsen, S. , ... Statom, N. (2023). Airborne Remote Sensing of Upper-Ocean and Surface Properties, Currents and Their Gradients From Meso to Submesoscales. *Geophysical Research Letters*, *50*(8), e2022GL102468. Retrieved 2023-05-22, from https://onlinelibrary.wiley.com/doi/abs/10.1029/2022GL102468 (_eprint: https://onlinelibrary.wiley.com/doi/pdf/10.1029/2022GL102468) doi: 10.1029/2022GL102468

Srinivasan, K., Barkan, R., & McWilliams, J. C. (2023). A Forward Energy Flux at Submesoscales Driven by Frontogenesis. *Journal of Physical Oceanography*, *53*(1), 287–305. Retrieved 2023-03-20, from https://journals.ametsoc.org/view/journals/phoc/53/1/JPO-D-22-0001.1.xml (Publisher: American Meteorological Society Section: Journal of Physical Oceanography) doi: 10.1175/JPO-D-22-0001.1

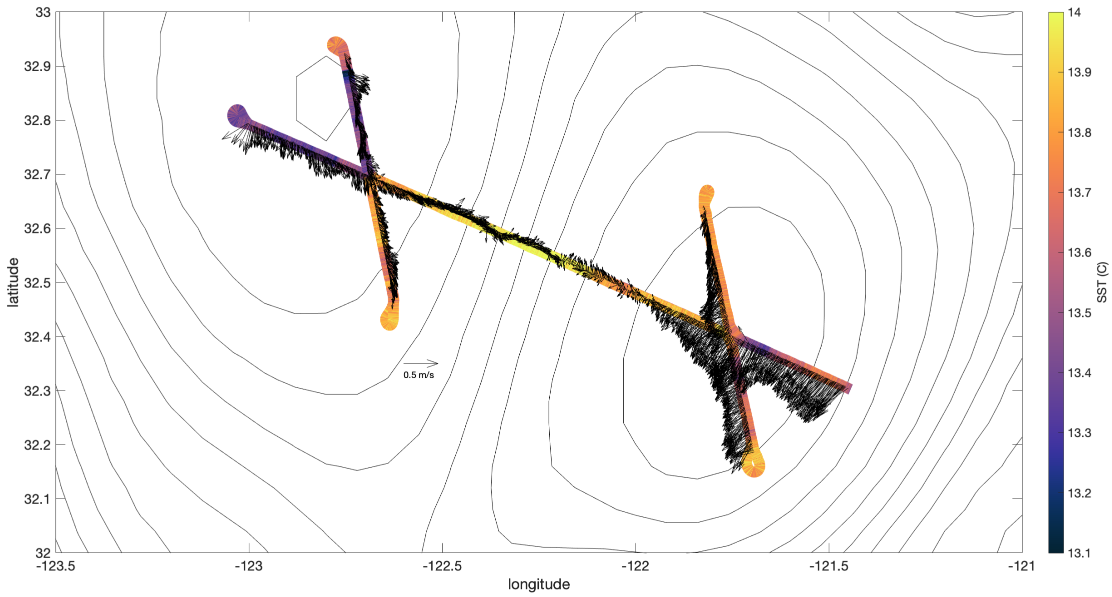

Figure S1. DoppVis velocity across the eddy region as vectors with sea surface temperature from the infrared thermometer. The contours are HYCOM sea surface height from May 19, 2021.

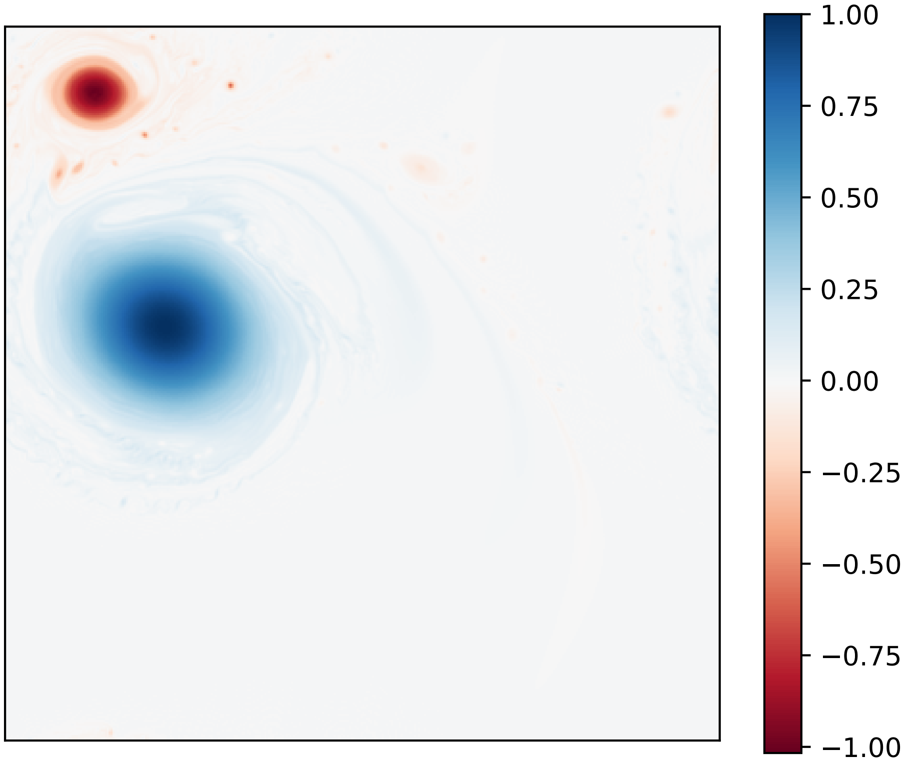

Figure S2. Snapshot of an SQG model initialized with an eddy and a filament. The SQG model used is PyQG. The model is non-dimensionalized with buoyancy frequency and Coriolis frequency equal, as is approximately the case in the surface layer here.

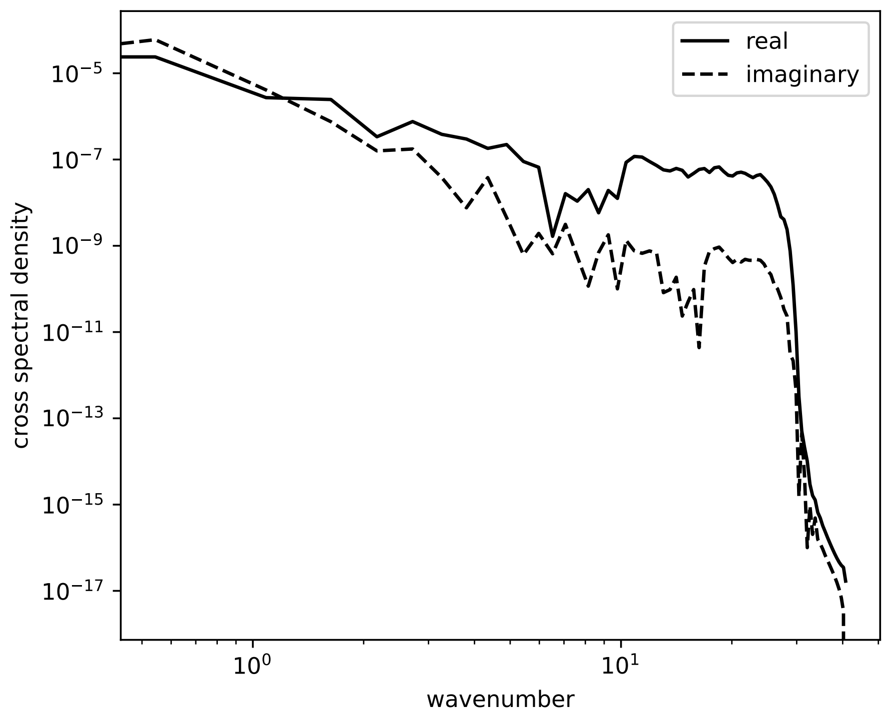

Figure S3. Cross spectrum as a function of wavenumber from a surface quasigeostrophic model initialized with two counter rotating eddies. The solid line is the real part of the cross spectrum while the dashed line is the imaginary part. In contrast to the observations where the imaginary part becomes relatively more important at small scales, in the SQG model the imaginary part becomes less important at small scales.

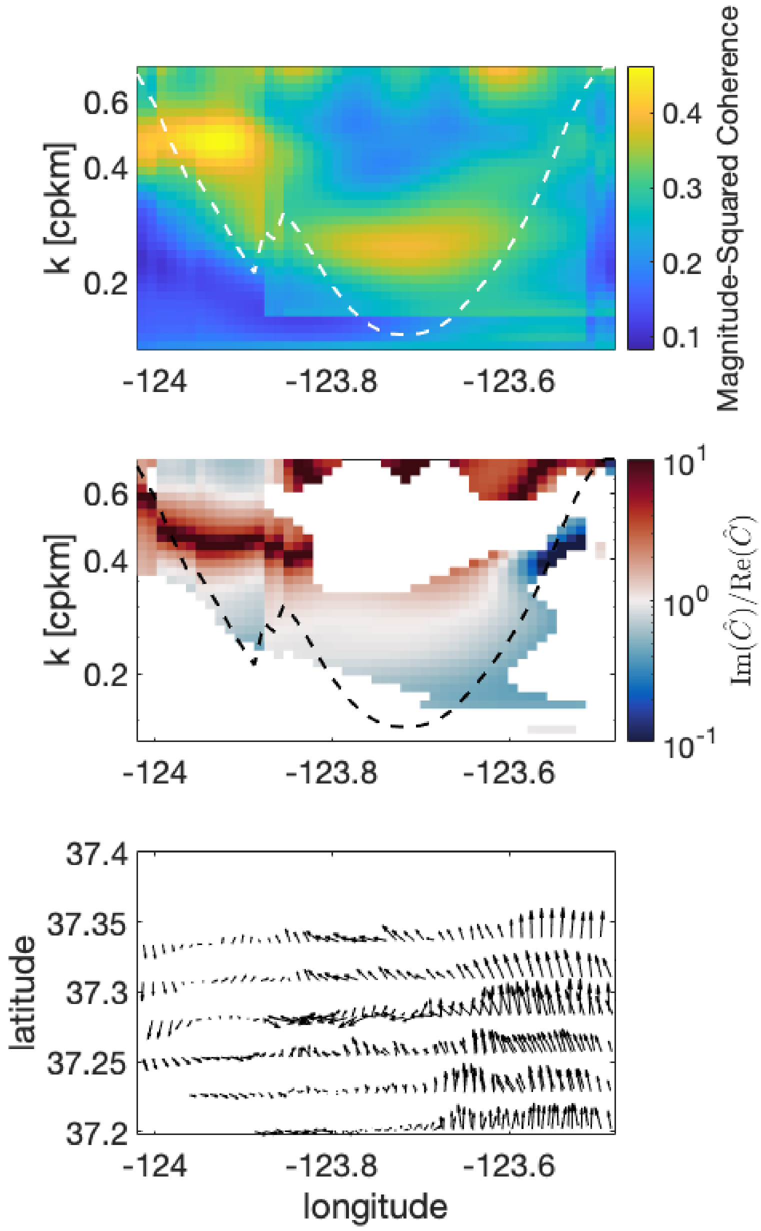

Figure S4. (top) Average wavelet coherence spectrum from S-MODE (middle) Ratio of the imaginary to real part of the cross spectrum. This ratio is only shown where the coherence value is above the significance threshold. (bottom) Velocity vectors. This analysis reveals that the shift from a predominantly real to a complex cross spectrum occurs at the strongest fronts in the region sampled, occurring at slightly larger scales at the western front and slightly smaller scales at the eastern fronts.

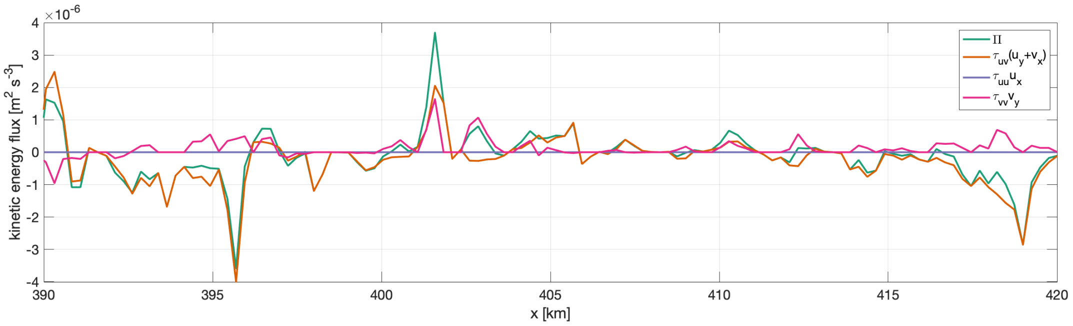

Figure S5. Kinetic energy flux across 1 km (Π) and its component parts $\Pi = -(\tau_{uv}(u_y + v_x) + \tau_{uu}u_x + \tau_{vv}v_y)$.

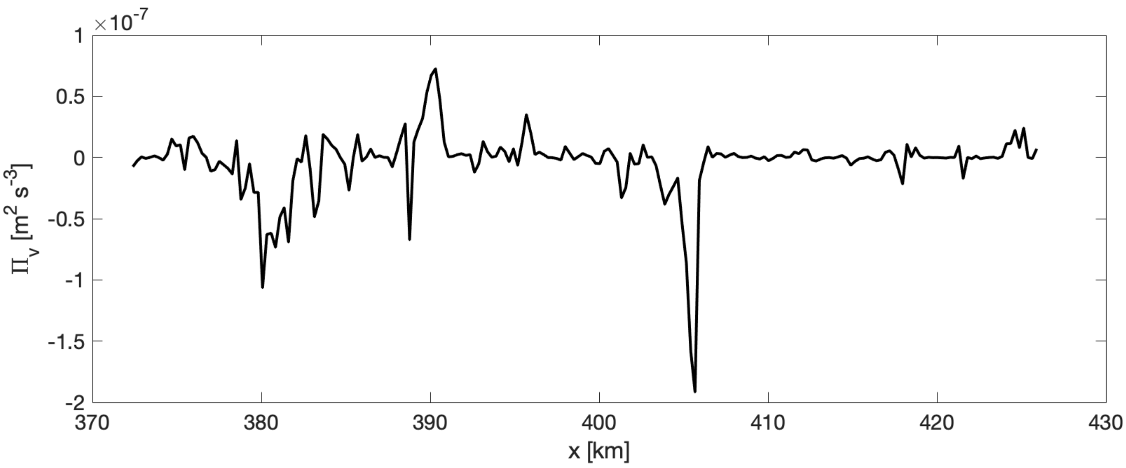

Figure S6. Kinetic energy flux associated with vertical shear Π_v across 1 km.